https://doi.org/10.1016/j.mechmachtheory.2023.105547

The novel synthesis of origami-inspired mechanisms based on graph theory

Zhihao Xia [a], Chunxu Tian [a], Luquan Li [a], Dan Zhang [a, b, *]
[a] Institute of AI and Robotics, Academy for Engineering & Technology, Fudan University, Shanghai, 200433, PR China
[b] Department of Mechanical Engineering, The Hong Kong Polytechnic University, Hong Kong, China

Abstract: In this paper, a novel synthesis approach based on graph theory is proposed. This approach can be used to design the creases of origami mechanisms. All possible contracted graphs of the 1-DOF origami mechanism are provided based on the number and graph synthesis methods. Then, a new method named loop synthesis is presented and this method is used to obtain different loop situations of the contracted graphs considering the structural characteristics of the origami mechanism. Two theorems are proposed and proven to determine the availability of loop situations. Furthermore, a modified thick panel design method for the origami mechanism is presented, and both single units and multiple units of the origami mechanism are modelled. At the same time, a rotary actuator based on this mechanism is introduced to verify the validity of the above synthesis approach. Finally, rotation, repeatability, and static torque tests are conducted to measure the inherent stiffness constant of the actuator. This approach, which was proven to be effective for designing the origami mechanism, can be readily applied to generate the desired mechanism.

Keywords: Generalized parallel mechanism, Origami mechanism, Graph theory, Contracted graph

1. Introduction

Origami mechanisms are unique engineered structures that draw inspiration from nature and the art of origami, offering exceptional flexibility, lightweight properties, and a wide range of potential applications. Mechanical engineers have successfully applied the core concepts of origami to practical engineering, transforming folded paper into innovative mechanical designs. Moreover, origami mechanisms can be used to design surgical instruments [1-3], buildings [4-6], and robots [7-9], thus providing distinctive solutions for both everyday life and specialized needs. In aerospace engineering, origami mechanisms enable the design of intricate foldable structures such as wings [10-12] and solar panels [13-15] for enhanced flexibility and efficiency in space exploration missions and communication satellites.

The origami mechanisms can be categorized into two distinct types: non-rigid and rigid origami mechanisms [16]. The former involves the utilization of flexible panels that can deform freely during the process of folding, commonly observed in applications such as umbrellas [17] and flexible solar wings. Conversely, the latter maintains its structural rigidity throughout the folding and unfolding processes, facilitating easier engineering control and prediction. Consequently, this aspect has garnered significant attention from academia. Since their inception, substantial advancements have been achieved in folding mechanisms. For instance, Miura [18] devised the Miura configuration to address the issue of folding and unfolding solar panels. This configuration has emerged as the most extensively investigated and implemented design. Xie et al. [19] introduced the hierarchical Miura-ori model, which was subsequently employed by Ma et al. [20] for structural designs featuring graded stiffnesses. Tachi [21] proposed a quadrangular grid origami pattern entirely composed of quadrangular panels. Within the four-crease vertex origami diagram lies a family of origami twists frequently utilized in the art to establish origami patterns [22]. It constitutes a crease graph comprising a central polygon and pairs of parallel creases radiating from each side [23]. This series of crease designs laid the groundwork for subsequent research and development of robots based on origami mechanisms.

However, in most cases, the development of origami mechanisms typically begins with a crease design followed by theoretical analysis [24]. In this approach, the design of an origami mechanism heavily relies on a moment of inspiration, making a crease design method crucially important. In the origami mechanism, creases can be considered revolute joints, and multiple creases at the same vertex can be seen as a spatial spherical parallel mechanism. Consequently, the crease design of an origami mechanism can be transformed into the structure synthesis of a generalized parallel mechanism [25-27]. Graph theory has been widely utilized in mechanism science due to its powerful capabilities and provides a structured approach for describing and analysing topological relationships within mechanisms [28,29]. Graph theory offers valuable theoretical support for mechanism synthesis by employing topological descriptions of linkages and joints. This methodology has been employed in numerous studies. Tian et al. [30] presented a systematic method for the structural synthesis of parallel manipulators with coupling sub-chains based on graph theory. He et al. [31] proposed a design method for hybrid mechanism configuration synthesis based on topological graph theory, which addresses the challenge of machining large and complex curved surfaces in the aerospace domain. Yang et al. [32] introduced a powertrain configuration scheme design method based on hierarchical topological graph theory. Additionally, many other scholars have also proposed some useful synthesis methods and different types of origami-inspired mechanisms [33-36].

In this paper, a novel synthesis approach for origami-inspired mechanisms based on graph theory is presented. In Section 2, starting from the topology of the origami mechanism, all contracted graphs are derived by the number and graph

---

[*] Corresponding author:
Dan Zhang, Email: dan.zhang@polyu.edu.hk

synthesis methods. Subsequently, a new method named loop synthesis is presented, and this method is used to obtain the different loop situations of the contracted graphs considering the structural characteristics of the origami mechanism. Then, two theorems for determining the availability of the loop situations are proposed, resulting in 72 valid loop situation graphs. In Section 3, a thick panel design for the origami mechanism is proposed, and both single units and multiple units of the origami mechanism are modelled. Additionally, a rotary actuator based on this mechanism is introduced. In Section 4, tests of the rotation, repeatability, and static torque are conducted to measure the inherent stiffness constant of the actuator. Conclusions are drawn in Section 5.

2. Origami mechanism synthesis

2.1. Number Synthesis and Graph Synthesis

The creases within an origami mechanism are utilized to facilitate the rotation of two interconnected rigid panels, thereby functioning as an equivalent to the revolute joint in the parallel mechanism. If we represent the crease of the origami mechanism as a line and each piece of rigid panel as a link connected by multiple lines, it becomes possible to describe the origami mechanism through a topological graph. This section will start with the degrees of freedom (DOFs) of the origami mechanism. Subsequently, a topological structure that fulfils the requirements of a rotary actuator is presented.

According to the aforementioned equivalent conditions, rigid panels with different fold numbers can be represented as distinct basic links: binary *B*, ternary *T*, quaternary *Q*, pentagonal *P*, or hexagonal *H* links [37]. The calculation of the DOFs in the origami mechanism is equivalent to solving for the DOFs in a parallel mechanism. By employing the modified Grübler-Kutzbach formula [38] and considering relevant conditions, it is easy to determine the DOFs in the origami mechanism as follows:

$$M = 6(n-g-1)+\sum_{i=1}^{g} f_i + \mu - \zeta \tag{1}$$

where *M* represents the DOFs of the origami mechanism, μ denotes the number of redundant constraints and ζ is the number of passive DOFs. n and g are defined as the total number of basic links and the total number of creases in the origami mechanism, and all kinematic joints are single DOF. Therefore, their calculation formulas are as follows:

$$n=\sum_{k=2}^{m} n_k \ , g=\sum_{i=1}^{g} f_i = \frac{1}{2}\sum_{k=2}^{m} k\cdot n_k \tag{2}$$

where n_k is the number of rigid panels with k creases. The number of independent loops V of the topological graph corresponding to the origami mechanism can be calculated through Euler's formula:

$$V = g-n+1=\frac{1}{2}(n_3+2n_4+3n_5+4n_6+\cdots)+1 \tag{3}$$

Substituting Eqs. (2) and (3) into Eq. (1) yields the quantity of *B* links:

$$n_2 = 5V-\sum_{k=3}^{m} n_k + \varphi \tag{4}$$

where $\varphi=M+\zeta-\mu+1$ is established.

Since the binary *B* link does not impact the connectivity in the topological graph, it is sufficient to consider the contracted graphs, and all the binary *B* links are removed. Since the rotary actuator only requires a single rotational DOF around a fixed axis and lacks a passive DOF, it satisfies M=1 and ζ=0. Commencing from situations with minimal independent loops, V=1/2/3/4 are selected, while the ternary *T*, quaternary *Q*, pentagonal *P*, and hexagonal *H* links serve as the basic links for constructing the contracted graphs. All situations that meet the conditions are listed in Table 1.

Table 1. Different combinations of basic links with *V*=1/2/3/4

V	No.	n_2	n_3	n_4	n_5	n_6	V	No.	n_2	n_3	n_4	n_5	n_6
1	1	$7-v$	0	0	0	0	4	9	$16-v$	6	0	0	0
2	2	$10-v$	2	0	0	0		10	$17-v$	4	1	0	0
	3	$11-v$	0	1	0	0		11	$18-v$	3	0	1	0
3	4	$13-v$	4	0	0	0		12	$18-v$	2	2	0	0
	5	$14-v$	2	1	0	0		13	$19-v$	2	0	0	1
	6	$15-v$	1	0	1	0		14	$19-v$	1	1	1	0
	7	$15-v$	0	2	0	0		15	$19-v$	0	3	0	0
	8	$16-v$	0	0	0	1		16	$20-v$	0	1	0	1
								17	$20-v$	0	0	2	0

The 29 situations presented in Table 1 are utilized to synthesize the contracted graphs of the origami mechanism. Taking No. 12 as an illustrative example comprising two *T* and two *Q* links, these four basic links are evenly distributed in a circular arrangement, and the adjacent links are connected in pairs. Based on permutation and combination principles, two situations can be distinguished: *TTQQ* and *TQTQ*. Subsequently focusing on *TTQQ*, apart from the edges connected to neighbouring links, one undetermined edge remains for Basic Link *T*, while two undetermined edges remain for Basic

Link *Q*. At this stage, Basic Link *T*, can be connected with either one of the *Q* links or another *T* link. Therefore, diverse contracted graphs can be obtained through different arrangements and combinations resulting in $n_{TTQQ} = C_2^1 C_2^1 + 1 = 5$. Fig. 1 shows all possible contracted graphs that do not contain self-loops.

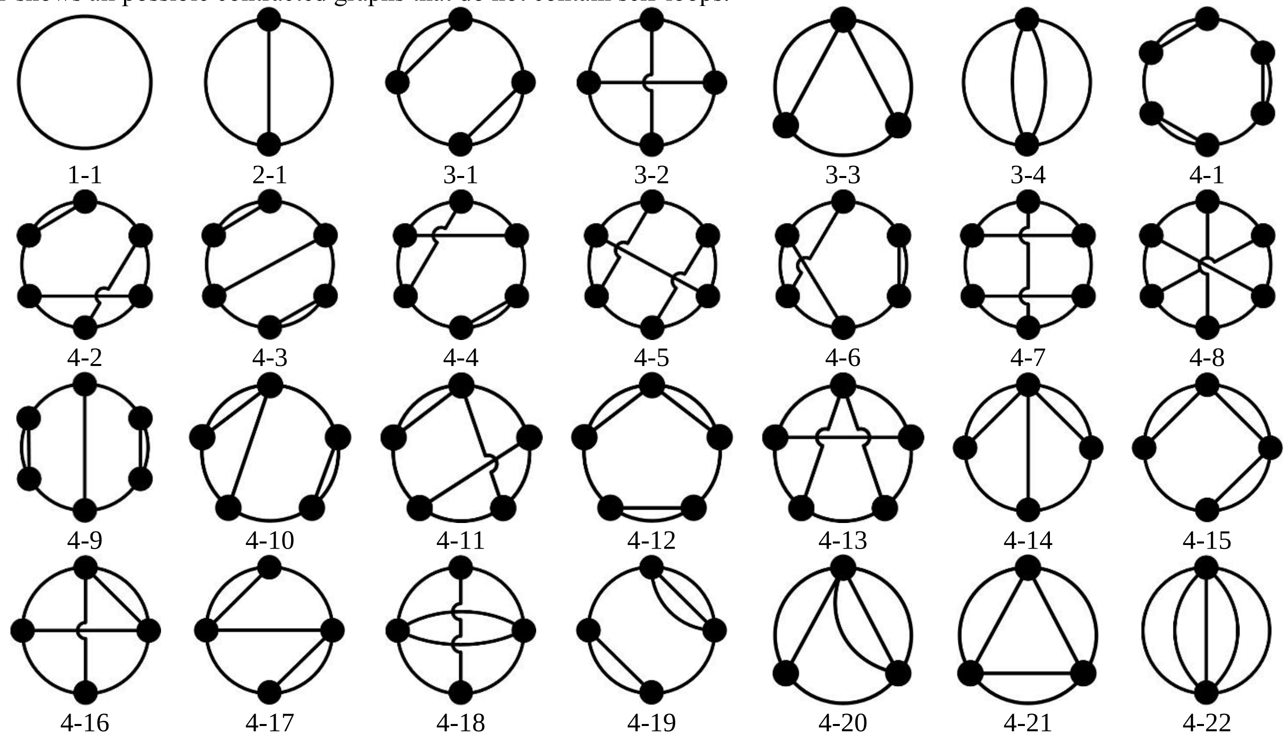
1-1 2-1 3-1 3-2 3-3 3-4 4-1
4-2 4-3 4-4 4-5 4-6 4-7 4-8
4-9 4-10 4-11 4-12 4-13 4-14 4-15
4-16 4-17 4-18 4-19 4-20 4-21 4-22

Fig. 1. All contracted graphs when the number of independent loops is *V*=1/2/3/4

To address the potential isomorphism between contracted graphs, the node response method (NRM) proposed by Xia et al. [39] is applied in this study to identify the isomorphism of contracted graphs. Compared with other existing methods, the NRM has higher accuracy. Even when the number of vertices is close to 30, the isomorphism judgement can still be completed. First, all nodes of the contracted graphs are numbered, with the top node designated as 1 and subsequent nodes assigned numbers in a counterclockwise order until all nodes are labelled. Subsequently, the NRM is applied to identify and remove isomorphic contracted graphs when comparing any two graphs. Finally, Fig. 2 illustrates all non-isomorphic contracted graphs.

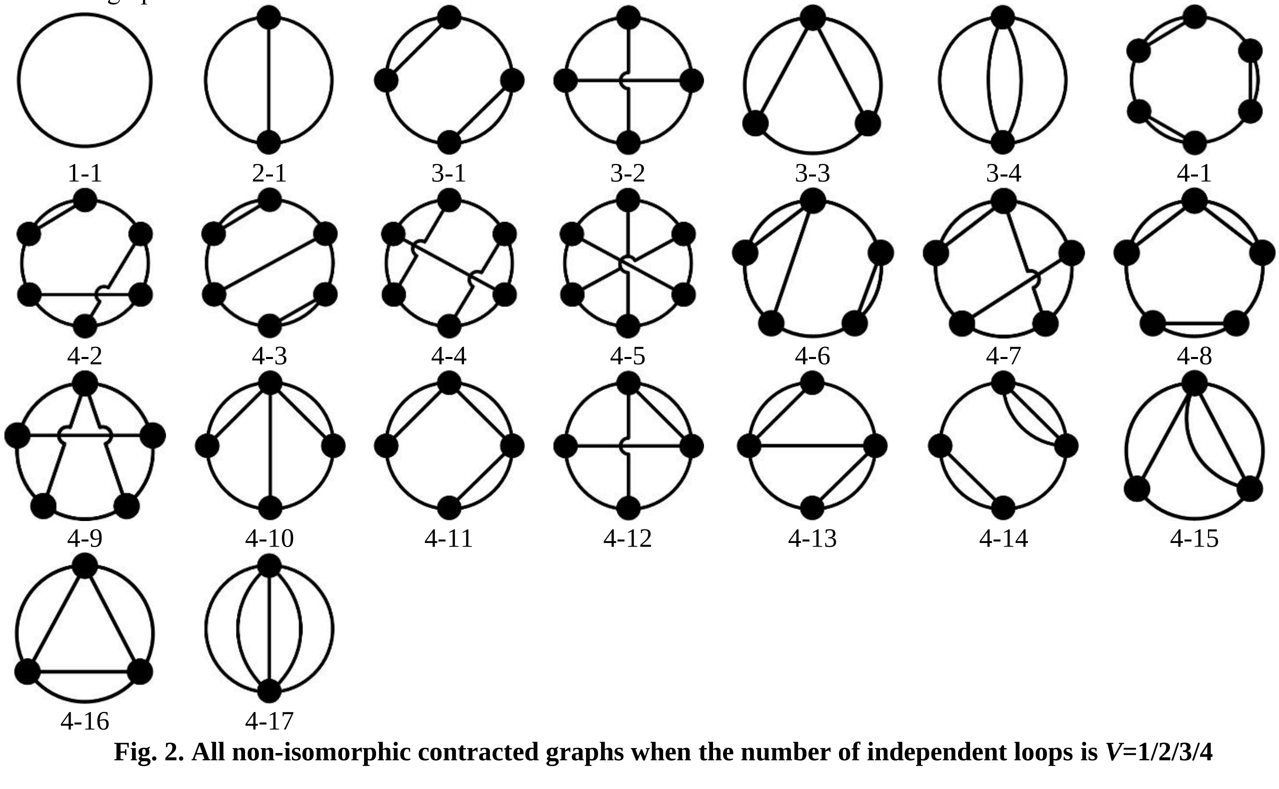
1-1 2-1 3-1 3-2 3-3 3-4 4-1
4-2 4-3 4-4 4-5 4-6 4-7 4-8
4-9 4-10 4-11 4-12 4-13 4-14 4-15
4-16 4-17

Fig. 2. All non-isomorphic contracted graphs when the number of independent loops is *V*=1/2/3/4

2.2. Loop synthesis

To achieve a specific origami mechanism, it is essential to determine both the fixed and moving platforms. Taking Fig. 2 (4-16) as an example, due to the rotational symmetry of the contracted graph, it appears that only one configuration can be formed, as shown in Fig. 3(a). However, an alternative configuration can be obtained by interchanging the order among different branches, as illustrated in Fig. 3(b).

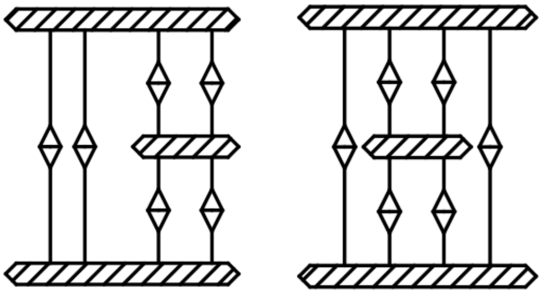

(a) Multiple rings outside (b) Multiple rings inside

Fig. 3. Different loop situations under the same contracted graph

To compare the differences between the aforementioned situations, it is necessary to establish the corresponding relationship between the origami mechanism and the topological graph. The Miura configuration shown in Fig. 4(a) represents a single DOF origami configuration [40], where each unit comprises four folds that intersect at a vertex. A red solid line denotes the mountain creases and dotted red lines represent valley creases, while the crease vertex is represented by a blue point. By representing the crease as a line and each rigid panel as a basic link, the contracted graph corresponding to the Miura configuration can be obtained, as shown in Fig. 4(b). The origami mechanism corresponding to the other contracted graphs in Figs. 1, 2, and 3 can also be obtained. By comparing the original configuration with its topological structure, it becomes evident that the vertices of multiple creases in the origami mechanism correspond to loops within the topological graph, precluding any presence of additional creases or basic links within these loops.

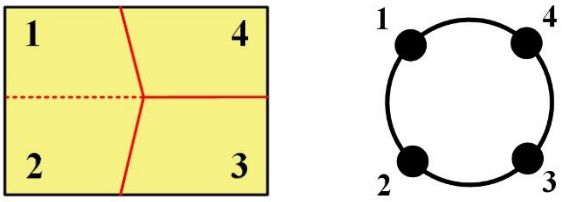

(a) Miura configuration (b) Topological graph of Miura

Fig. 4. Miura configuration and its topological graph

Loops V_i, Basic Links N_i, and Connections C_i are numbered for the convenience of observation. Based on the aforementioned corresponding relationship, the origami mechanisms corresponding to the two situations shown in Fig. 3 can be derived as illustrated in Fig. 5. It is obvious that the two origami mechanisms in Fig. 5 are different.

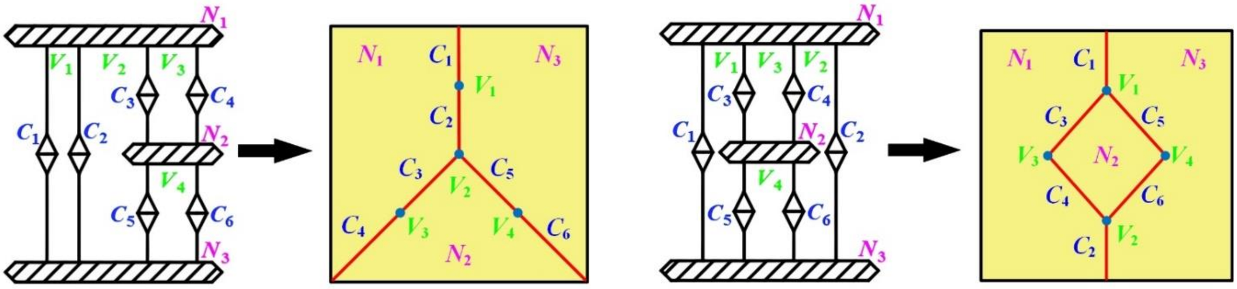

(a) Multiple rings outside (b) Multiple rings inside

Fig. 5. Origami mechanisms under different loop situations

Therefore, to miss any loop situations during the structure synthesis of the origami mechanism, the loop synthesis of contracted graphs will be conducted. Taking Fig. 2 (4-3) as an example, each basic link is numbered, as shown in Fig. 6(a). Assuming that Basic Link 1 and Basic Link 2 serve as a moving platform and a fixed platform, one possible loop situation is illustrated in Fig. 6(b), with each connection represented by a straight line. It can be observed that there are three branches between Basic Link 1 and Basic Link 2, where the two left branches are identical. By rearranging the order of these three branches, $C_3^1 = 3$ different situations can be obtained, while the remaining two situations are shown in Figs. 6(c) and 6(d). Furthermore, it becomes apparent that the rightmost branch in Fig. 6(b) comprises two sub-branches. Since these sub-branches differ, interchanging their order results in $C_2^1 = 2$ loop situations. Consequently, $C_3^1 C_2^1 = 6$ loop situations can be obtained for the contracted graph. The remaining situations are illustrated in Figs. 6(e), 6(f) and 6(g).

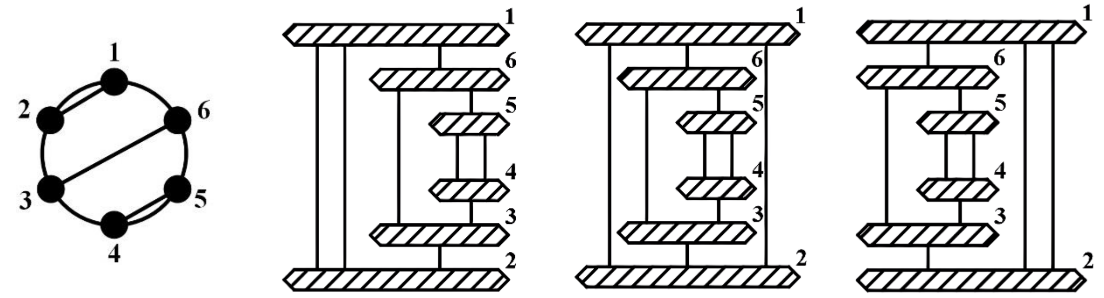

(a) The contracted graph (b) Situation 1 (c) Situation 2 (d) Situation 3

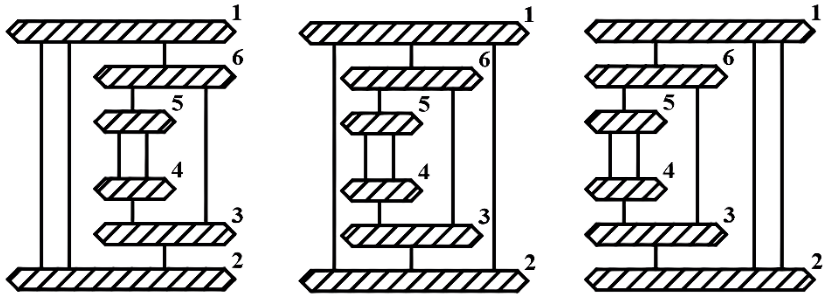

(e) Situation 4 (f) Situation 5 (g) Situation 6

Fig. 6. Different loop situations under the same contracted graph

To eliminate the same loop situation, statistical analyses of the six situations are conducted, and the basic links required to form the loop are recorded, as shown in Eq. (5):

$$\begin{cases} V_{1-2}, V_{1-2-3-6}, V_{3-4-5-6}, V_{4-5} \\ V_{1-2-3-6}, V_{3-4-5-6}, V_{4-5}, V_{1-2-3-4-5-6} \\ V_{3-4-5-6}, V_{4-5}, V_{1-2-3-4-5-6}, V_{1-2} \\ V_{1-2}, V_{1-2-3-4-5-6}, V_{4-5}, V_{3-4-5-6} \\ V_{1-2-3-4-5-6}, V_{4-5}, V_{3-4-5-6}, V_{1-2-3-6} \\ V_{4-5}, V_{3-4-5-6}, V_{1-2-3-6}, V_{1-2} \end{cases} \tag{5}$$

where $\boldsymbol{V_{i\text{-}j}}$ is represented as a loop composed of Basic Link $\boldsymbol{i}$ and Basic Link $\boldsymbol{j}$, and each row represents one loop situation in Fig. 6. Since only the order of the branches is adjusted during the loop synthesis, it is considered a repetition only if all loop compositions are the same. By observing Eq. (5), it is not difficult to find that the loop compositions of Fig. 6(b) and Fig. 6(g), Fig. 6(c) and Fig. 6(f), and Fig. 6(d) and Fig. 6(e) correspond to the same scenario. Therefore, the only truly valid loop situations are Figs. 6(b), 6(c) and 6(d).

For other contracted graphs, the same approach can be used for loop synthesis. Based on the above description, the general steps of loop synthesis are given below:

(1) Select any two basic links as the fixed platform and moving platform;

(2) Check all branches between two platforms and exchange the order between branches;

(3) Determine whether there are sub-branches within each branch. If they exist, exchange the order between the sub-branches; otherwise, proceed to Step 5;

(4) Repeat Step 3 continuously.

(5) Record the loop composition of each situation and remove duplicate loop situations.

2.3. The availability verification of contracted graphs

A large number of loop situations can be obtained through loop synthesis, but not all situations are satisfied. Thus, it is necessary to establish some theorems for eliminating invalid situations. The two specific theorems are presented and proven below.

Theorem 1. A contracted graph has only one common connection between two adjacent loops.

Proof 1. In a contracted graph, adjacent loops necessarily share at least one common connection. The following proof by contradiction demonstrates that adjacent loops can have at most one shared connection. It is assumed that there are n common connections and two independent connections between two adjacent loops V_1 and V_2, represented as C_i, where $n \geqslant 2$ and $i=1 \to n+2$ are satisfied, as shown in Fig. 7(a). Since Connection C_i ($i=1 \to n$) and Adjacent Loops V_1 and V_2 belong to common creases and crease vertices in the corresponding origami mechanism, respectively, each end of every crease is connected to Vertices V_1 and V_2. Simultaneously, considering that all creases are line segments with fixed lengths, these shared creases can only represent the same crease within the origami mechanism. Hence, there can be at most one shared connection between two adjacent loops. This contradicts the assumption. Thus, **Theorem 1** is established.

Theorem 2. A contracted graph cannot have adjacent connections between two basic links.

Proof 2. The following proof by contradiction demonstrates that adjacent connections cannot exist between two basic links. It is assumed that there are adjacent connections between two basic links. As shown in Fig. 7(b), C_1, C_2, and C_3 are three connections between two basic links, where C_1 is adjacent to C_2, and C_2 is adjacent to C_3. V_1 and V_2 are loops composed of these three connections. To ensure relative movement between the two basic links, Creases C_1 and C_2 need to be coaxial, and Creases C_2 and C_3 need to be coaxial. Therefore, Creases C_1, C_2, and C_3 can only represent one crease. That is, there cannot be adjacent connections between two basic links. This contradicts the assumption. Thus, **Theorem 2** is established.

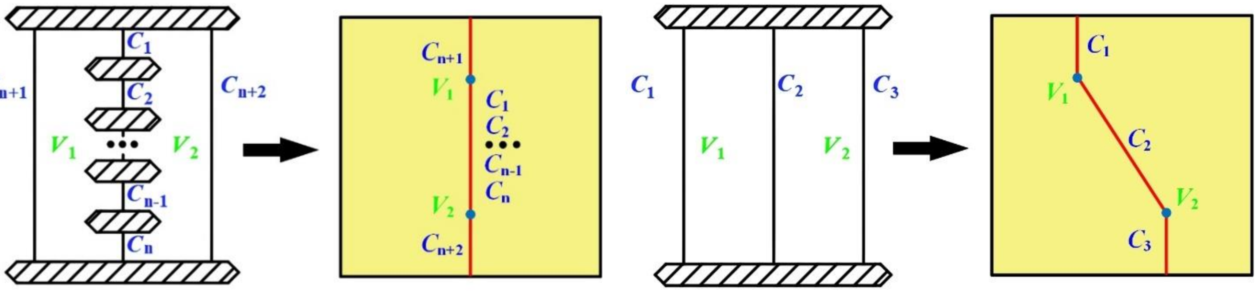

(a) Theorem 1 (b) Theorem 2

Fig. 7. Two different theorems

Subsequently, the two theorems mentioned above are applied to evaluate the availability of Figs. 6(b), 6(c) and 6(d). First, the numerical labels of C_i and V_i are assigned to all connections and loops, respectively, as shown in Fig. 8. In Fig. 8(a), C_1 and C_2 do not seem to satisfy **Theorem 2**, and thus, another situation needs to be considered. Since Fig. 8 shows a contracted graph, the possibility of the binary B links on the connections cannot be ruled out. The binary B links cannot exist on C_2 without violating **Theorem 1** since it serves as the common connection between V_1 and V_2. Conversely, since C_1 is an independent connection of V_1, introducing the binary B links onto C_1 satisfies **Theorem 2**. Thus, Fig. 8(a) is an available contracted graph. In Fig. 8(b), V_1 and V_4 have common connections with C_3 and C_9. Meanwhile, V_2 and V_4 have common connections with C_5 and C_8. At the same time, since C_6 and C_7 are the public connections of V_2 and V_3, V_3 and V_4, respectively, the binary B link does not exist on C_6 and C_7. Therefore, **Theorem 2** is not satisfied. This results in Fig. 8(b) not being an available contracted graph. Similarly, Fig. 8(c) is not an available contracted graph.

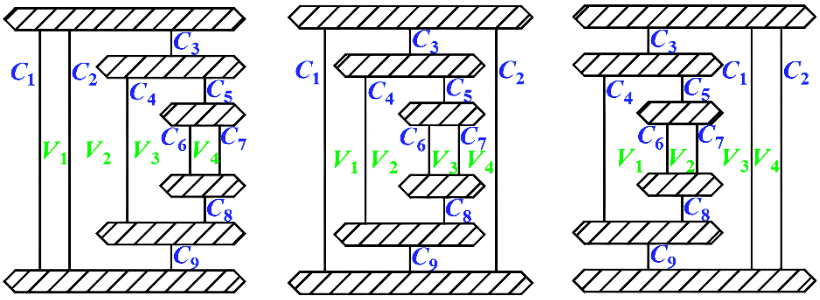

(a) Situation 1 (b) Situation 2 (c) Situation 3

Fig. 8. Numbered contracted graphs

After excluding unavailable loop situations, a total of 72 available loop situations are obtained, as presented in Appendix I. In this paper, only five symmetric loop situations are retained to ensure uniform force distribution on each branch of the origami mechanism, as shown in Fig. 9.

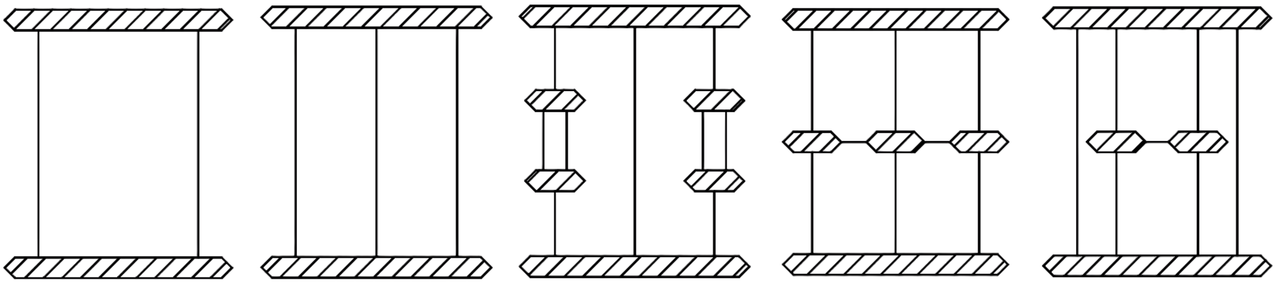

(a) 1-1 (b) 2-1 (c) 3-1 (d) 3-2 (e) 3-3

Fig. 9. Five symmetric available loop situations

According to the definition of flat-foldable single-vertex crease patterns provided in the literature [41], a single-vertex crease pattern defined by the angles $\theta_1+\theta_2+\ldots+\theta_n=360°$ is flat foldable if and only if n is even and the sum of the odd angles θ_{2i+1} is equal to the sum of the even angles θ_{2i}, or equivalently, either sum is equal to 180°. Consequently, for synthesizing a complete origami mechanism, adding some binary B links into the contracted graphs becomes necessary. To maintain simplicity within the mechanism design, adding as few binary *B* links as possible is preferable while ensuring an even number of basic links in a single loop. However, since the topological graph must also satisfy **Theorem 1** and **Theorem 2**, it is evident that 3-3 shown in Fig. 9 cannot fulfil all requirements for forming an available topological graph. After adding binary *B* links, the topological graphs of the remaining four cases have corresponding origami mechanisms, as shown in Fig. 10. Additionally, some asymmetric topological graphs and their corresponding origami mechanisms are shown in Fig. 11.

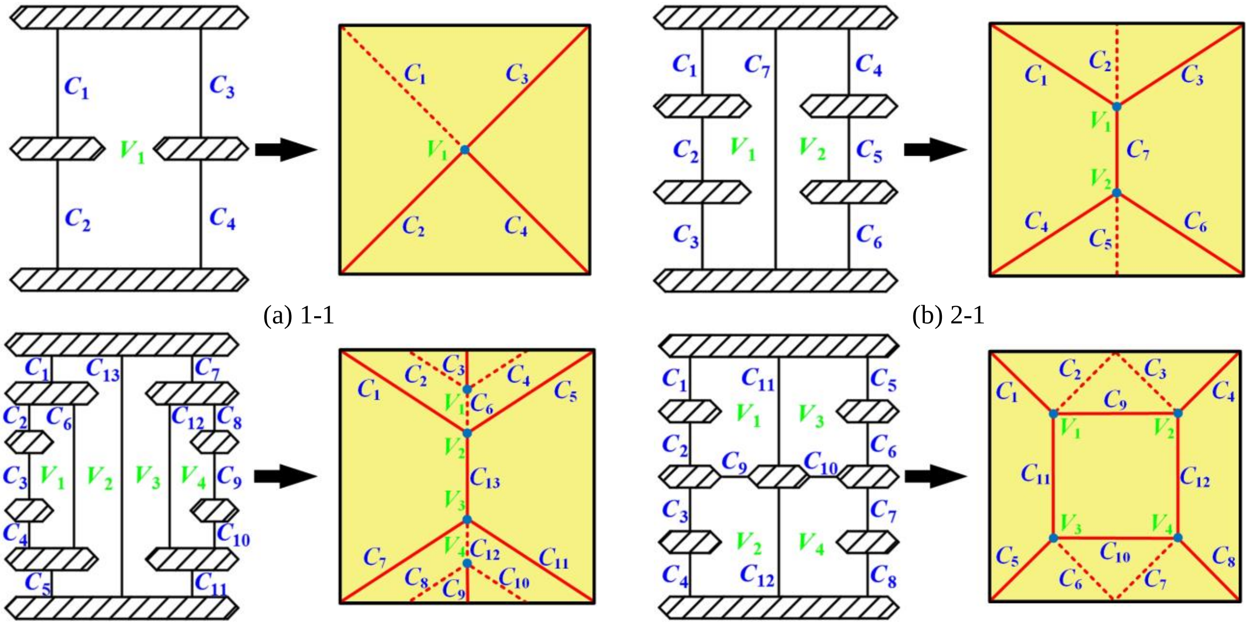

(a) 1-1

(b) 2-1

(c) 3-1

(d) 3-2

Fig. 10. Four available topological graphs and their origami mechanisms

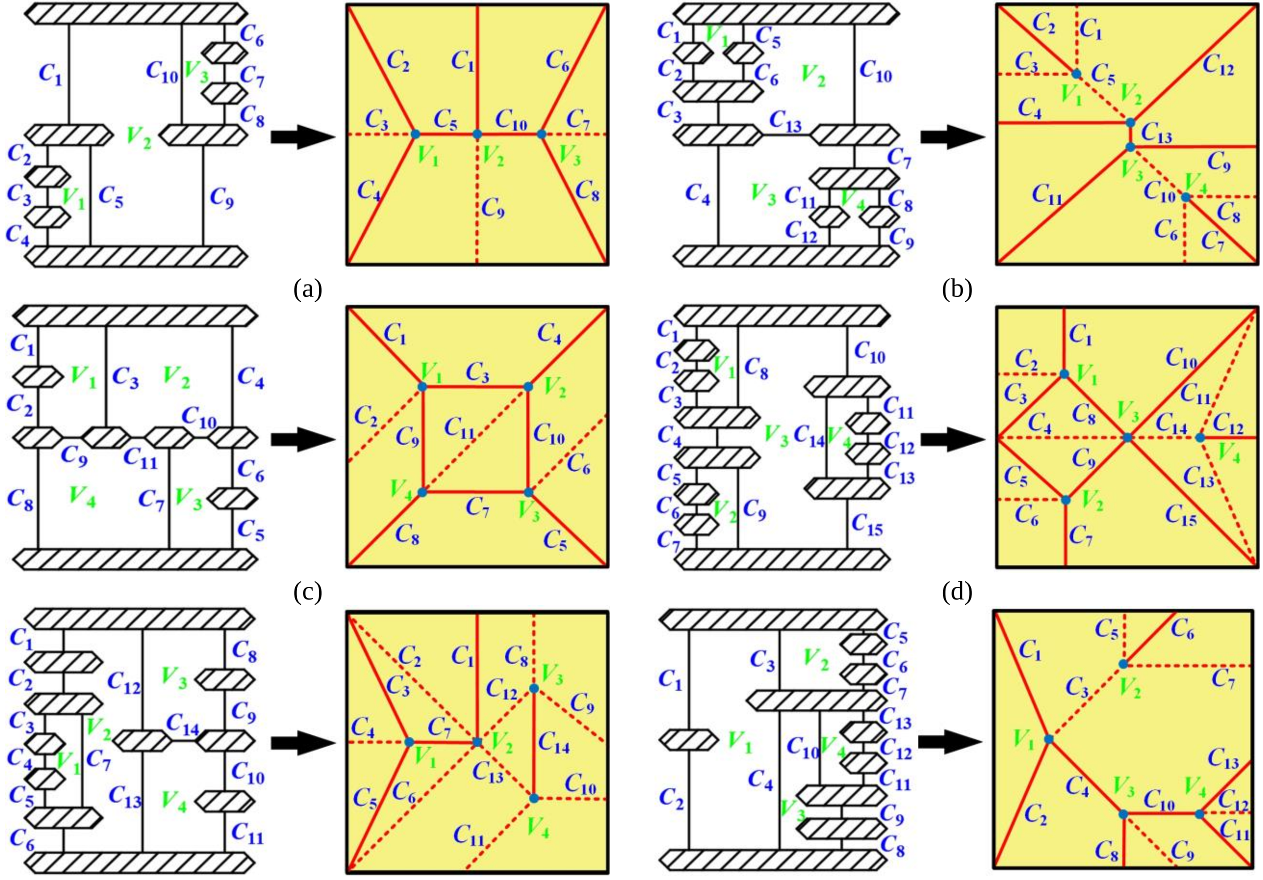

(a)

(b)

(c)

(d)

(e)

(f)

Fig. 11. Some asymmetric topological graphs and their origami mechanisms

2.4. Structure synthesis

Based on the four available origami mechanisms obtained in Fig. 10, the structural units of the rotary actuator are synthesized. The rotary actuator has only one rotational motion around a fixed axis, which results in the need to ensure this motion mode between the moving platform and the fixed platform of each unit. Therefore, 1-1 and 3-2 in Fig. 10 are eliminated, and 2-1 with a simpler structure is selected for synthesis.

To avoid interference between the origami mechanism and the central rotation axis, 2-1 in Fig. 10 is appropriately cut, as shown in Fig. 12(a). The green dotted line represents the cropping boundary, and the white area represents the cropped part. For the trimmed mechanism, since its two branches are spherical mechanisms with different intersection points, this ensures that the whole origami mechanism is still a single DOF rotation mechanism. At the same time, to increase the stiffness of the mechanism, as shown in Fig. 12(b), an origami mechanism that is folded inward is added to ensure that it does not shift in the axial direction. The three creases introduced in the cropped section are parallel to each other, thus, the motion of the origami mechanism is not constrained.


(a) After cut (b) The final mechanism

Fig. 12. Origami mechanism with a single DOF rotating around a fixed axis

Some constraints need to be added to avoid the interference caused by the origami mechanism during the folding process and simultaneously achieve a more compact folded mechanism. Among them, the three branches cannot overlap after flat-folding, which is a necessary but insufficient condition for the origami mechanism not to interfere. Since the origami mechanism in Fig. 12(b) is a symmetrical figure, only the upper left quarter is analysed. The structure parameters of the origami mechanism are shown in Fig. 13(a). To ensure that each side of the origami mechanism overlaps after being folded, it is also necessary to ensure that the three branches cannot overlap and reach the state in Fig. 13(b). The constraints are provided as follows:

$$\begin{cases} \angle 1 = \angle 2 \\ L_2 = L_3 \\ L_1 + L_5 / 2 = L_2 + L_4 / 2 \end{cases} \tag{6}$$

(a) Structure parameters (b) Folded state

Fig. 13. Origami mechanism and its folded state

3. Modelling of the rotary actuator

The thickness of the origami mechanism is not considered during the design process in the previous section. However, in the actual manufacturing process, the thickness of the material often cannot be ignored. In this section, to ensure that the thick origami mechanism has the same motion characteristics as the thickness origami mechanism, the corresponding thick origami mechanism is designed, and the rotary actuator is modelled.

3.1. Thick origami design

To achieve the folding motion of the origami mechanism under thick panels, some mainstream methods such as tapered panel [42], axis-shift joint [43], and planar compliant joint [44] technologies are implemented. Since each method has a unique applicability, they cannot be directly applied to the origami mechanism designed in this paper. To satisfy the requirements of the origami mechanism, the structure can be compactly folded while ensuring the original motion characteristics. In this section, axis-shift joint technology and tapered panel technology are combined to meet the design requirements.

The procedure for creating thick panels is as follows. First, a zero-thickness ideal origami is thickened by offsetting the surface by a constant distance in two directions, as shown in Fig. 14.

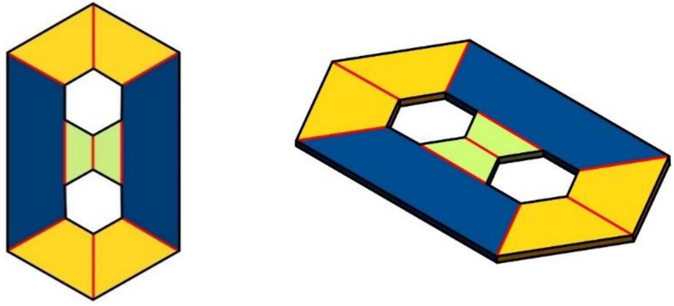

(a) Zero-thickness ideal origami (b) Thick origami

Fig. 14. Zero-thickness ideal origami and thick origami

Then, through the axis-shift joint technology, the mountain folds are arranged to the lower surface of the origami mechanism, and the valley folds are arranged to the upper surface of the origami mechanism. The thick blue panels on both sides are used as the fixed and moving platforms, respectively. The folding process of the origami mechanism is shown in Fig. 15(a). From left to right, the angles of the origami mechanism are 0°, 30°, 45°, 60° and 90°. By observing the folding process of the origami mechanism, it can be found that the axis formed by the plane of the fixed platform and the moving platform will change its position as the folding angle changes. As shown in Fig. 15(b), the axis position will be at infinity when the origami mechanism is completely folded. This shows that the origami mechanism does not rotate around a fixed axis during the folding process. Thus, this cannot satisfy the design requirements of the rotary actuator.

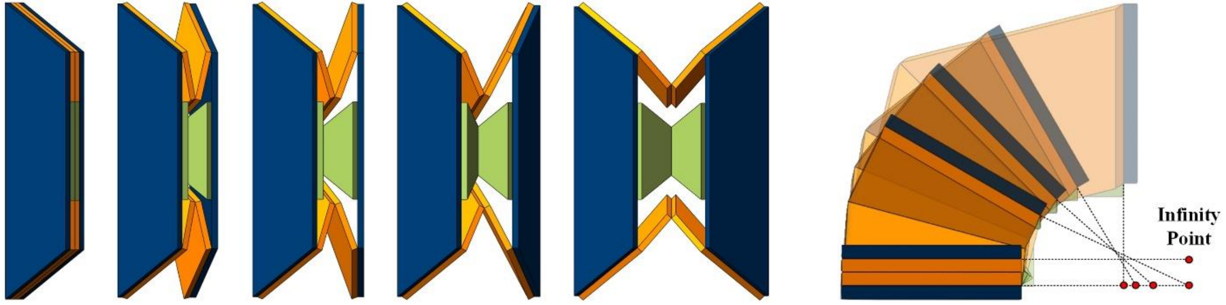

(a) The folding process of the origami mechanism (b) The axis of the origami mechanism

Fig. 15. Folding process of the origami mechanism based on axis-shift joint technology

To solve the above problem, tapered panel technology is used to redesign the crease position in the origami mechanism. As shown in Fig. 16(a), first, when the origami mechanism is completely folded, Plane $\boldsymbol{\Omega}$, which passes through the middle crease in the two branches at the same time, is determined. Next, all the creases are projected onto Plane $\boldsymbol{\Omega}$, and two intersection points formed by the projection of the creases are obtained. Then, the two intersection points are connected to obtain the rotation axis $\boldsymbol{L_R}$ of the rotary actuator. Three planes $\boldsymbol{\alpha}$, $\boldsymbol{\beta}$, and $\boldsymbol{\gamma}$ are created through the rotation axis $\boldsymbol{L_R}$, among which Plane $\boldsymbol{\beta}$ coincides with Plane $\boldsymbol{\Omega}$, and Plane $\boldsymbol{\alpha}$ and Plane $\boldsymbol{\gamma}$ are centrally symmetrical with Plane $\boldsymbol{\beta}$. As shown in Fig. 16(b), these three planes re-segment the original origami mechanism, forming new creases.

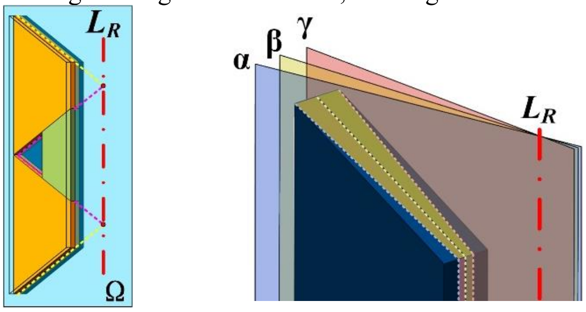

(a) Rotation axis (b) Split plane

Fig. 16. Redesign of the origami mechanism based on tapered panel technology

After the creases are redesigned, the folding process of the origami mechanism is shown in Fig. 17(a). From left to right, the angles of the origami mechanism are 0°, 30°, 45°, 60° and 90°. By observing the folding process of the origami mechanism, it can be found that the axis formed by the plane of the fixed platform and the moving platform is fixed. As shown in Fig. 17(b), a spatial spherical mechanism is formed since the three creases of the branches on any side intersect at the same point. This ensures that the origami mechanism can rotate around the fixed axis $\boldsymbol{L_R}$ regardless of the folding angle.

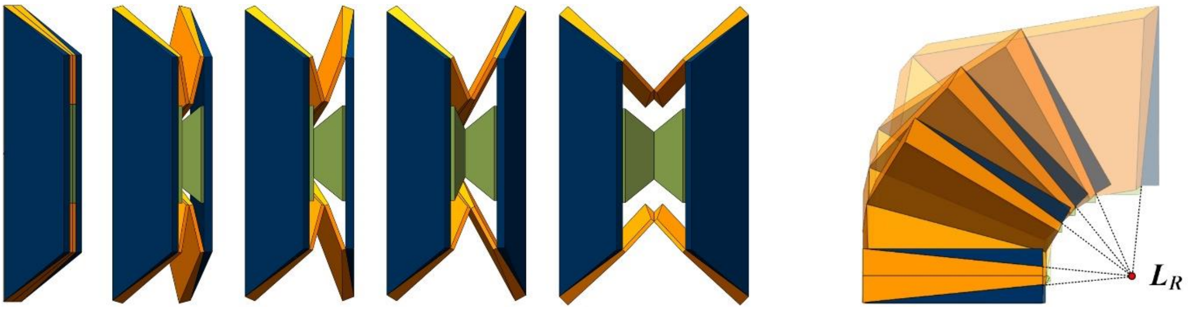

(a) The folding process of the origami mechanism (b) The axis of the origami mechanism

Fig. 17. Folding process of the origami mechanism based on tapered panel technology

3.2. Single unit

To describe the motion of the origami mechanism mathematically, it is necessary to analyse the geometric relationship of the mechanism. After the creases are redesigned, the parameters of the origami mechanism are shown in Fig. 18. For the convenience of display, Fig. 18(b) is the left view after the fixed platform is hidden.

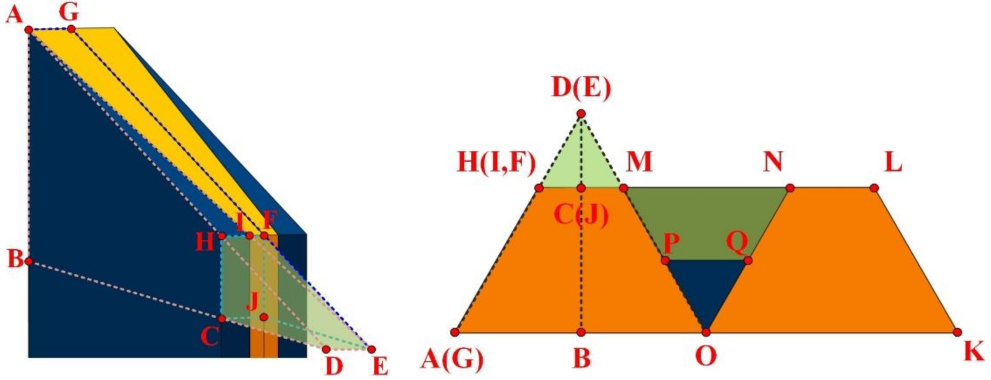

(a) Axonometric drawing (b) Left view

Fig. 18. Parameters of the origami mechanism

Assuming that the initial thickness of the origami mechanism is t, then the thickness of one side after folding is $2t$, that is:

$$L_{AG} = L_{DE} = L_{CJ} = L_{FH} = L_{HI} + L_{FI} = 2t \tag{7}$$

where L_{XX} represents the length of Line Segment XX. To obtain the specific thickness L_{HI} and L_{FI} of each panel after segmentation, according to the geometric relationship, the following equations are derived:

$$\begin{cases} \dfrac{L_{HI}}{L_{DE}} = \dfrac{L_{AH}}{L_{AH} + L_{DH}} \\[2ex] \dfrac{L_{CD}}{L_{BC} + L_{CD}} = \dfrac{L_{DH}}{L_{AH} + L_{DH}} \end{cases} \tag{8}$$

where $L_{CD}=L_{EJ}=a$ is the distance from the rotation axis to the origami mechanism, and $L_{BC}=b$ is the radial width of the origami mechanism. L_{HI} and L_{FI} can be obtained by adding the two equations of Eq. (8):

$$\begin{cases} L_{HI} = \dfrac{L_{DE} \cdot L_{BC}}{L_{BC} + L_{CD}} = \dfrac{2tb}{b+a} \\[2ex] L_{FI} = 2t - L_{HI} = \dfrac{2ta}{b+a} \end{cases} \tag{9}$$

Assuming that the tilt angle is θ, using trigonometric functions, the dimensions L_{AH}, L_{KL}, $L_{AK,}$ and L_{HL} of the fixed platform and the moving platform can be obtained. Since the origami mechanism is symmetrical on both sides, $L_{AH}=L_{KL}$ and $L_{AK}=2L_{AO}=4L_{AB}$ are established. Finally, the structural parameters of the fixed platform and the moving platform are as follows:

$$\begin{cases} L_{AH} = L_{KL} = \dfrac{L_{BC}}{\cos\theta} = \dfrac{b}{\cos\theta} \\ L_{AK} = 4L_{AB} = 4(L_{BC} + L_{CD})\tan\theta = 4(b+a)\tan\theta \\ L_{HL} = L_{AK} - 2L_{AH}\sin\theta = 2(b+2a)\tan\theta \end{cases} \tag{10}$$

In the same way, the structural parameters L_{MP}, L_{NQ}, $L_{MN,}$ and L_{PQ} of the intermediate branch can be obtained:

$$\begin{cases} L_{MP} = L_{NQ} = \dfrac{L_{CD}}{\cos\theta} = \dfrac{a}{\cos\theta} \\ L_{MN} = 2L_{BC}\tan\theta = 2b\tan\theta \\ L_{PQ} = L_{MN} - 2L_{MP}\sin\theta = 2(b-a)\tan\theta \end{cases} \tag{11}$$

3.3. Multi-unit

By rigidly connecting the former unit's moving platform to the latter unit's fixed platform, multiple units can be connected end to end, forming a multi-unit. Fig. 19 shows the specific connection between the units.

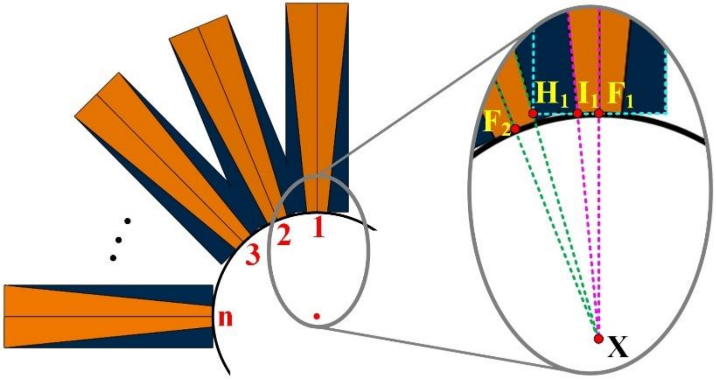

Fig. 19. Multi-unit stacking

Point X on the rotation axis $\boldsymbol{L_R}$ is taken as the centre of the circle, and L_{F_1X} is taken as the radius of the circle. Each unit is evenly distributed on the circumference, and Points F_1 and F_2 are the tangent points of the Circle X. Without reducing the volume of the fixed platform and the moving platform, the two units should be as close as possible. The angle $\angle F_1XF_2$ between the two units is defined as φ. Then, the following can be obtained:

$$\varphi = \angle F_1XI_1 + \angle H_1XI_1 + \angle F_2XH_1 \tag{12}$$

where $\angle F_1XI_1 = \angle F_2XH_1$, $L_{F_1X} = L_{EJ} = a$ and $L_{F_1I_1} = L_{FI}$ are established. Since $F_1X \perp F_1I_1$ is satisfied, the following equation can be obtained:

$$\angle F_1XI_1 = \angle F_2XH_1 = \arctan(\frac{L_{F_1I_1}}{L_{F_1X}}) = \arctan(\frac{2t}{b+a}) \tag{13}$$

In the same way, because $L_{F_1H_1} = L_{FH}$ is satisfied, the following equation can be obtained:

$$\angle H_1XI_1 = \angle F_1XH_1 - \angle F_1XI_1 = \arctan(\frac{L_{F_1H_1}}{L_{F_1X}}) - \angle F_1XI_1 = \arctan(\frac{2t}{a}) - \arctan(\frac{2t}{b+a}) \tag{14}$$

Substituting Eqs. (13) and (14) into Eq. (12) yields $\angle F_1XF_2$:

$$\varphi = \arctan(\frac{2t}{a}) + \arctan(\frac{2t}{b+a}) \tag{15}$$

3.4. Fabrication of the rotary actuator

A plastic film that is wrapped on the outside and a rigid origami mechanism that is found on the inside are used to form a soft airbag for pneumatic driving [45]. To complete the manufacturing of the rotary actuator, four steps are needed, as shown in Fig. 20. The detailed fabrication process is as follows:

(1) 3D printing technology is used to print the origami mechanism, and Teflon tape is used to connect the creases to complete the production of the rigid skeleton;

(2) Two pieces of PVC film are used to wrap the rigid skeleton from the upper and lower sides, they are fitted as closely

as possible;

(3) Thermoplastic sealing technology is used to seal the film contact points, and the air inlet and outlet holes are then retained;

(4) The excess part is removed, the film is fixed to the rigid skeleton, and the overall airtightness check is completed.

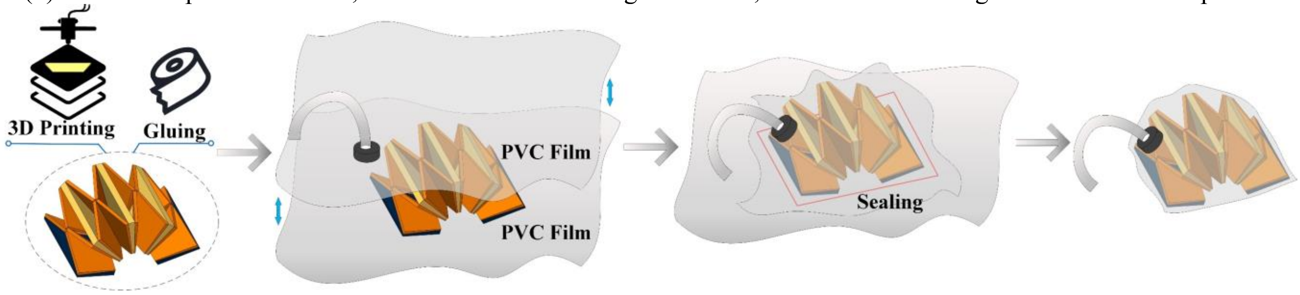

Fig. 20. Fabrication of the rotary actuator

The rotary actuator uses compressed air for joint rotation. The fully folded position of the actuator is defined as a rotation angle of 0. By changing the internal air pressure, the actuator can rotate between the working space [0, α] with a torque T. By using the trapezoidal $AILK$ as the force-bearing surface to simplify the inflatable structure, the torque T generated by the actuator can be obtained as follows:

$$\begin{aligned} T &= -k\alpha + \int_a^{a+b} (P - P_0) \frac{r \cdot L_{AK}}{a+b} r dr \\ &= -k\alpha + \int_a^{a+b} (P - P_0) r^2 \tan\theta dr \\ &= -k\alpha + \frac{1}{3}(P - P_0)\tan\theta[(a+b)^3 - a^3] \end{aligned} \tag{16}$$

where P_0 is the standard atmospheric pressure, P is the internal air pressure of the actuator, and k is an inherent stiffness constant, which depends on the actuator's material and structure and is determined by calibration.

4. Experiment Validation

4.1. Experimental Setup

The actuator designed in Section 2 and Section 3 on the correlations of the torque, stiffness, angle, and pressure are validated in this section. The rotation range of each unit is set to [0, ϕ]. That is, the rotation range of the entire actuator is $\alpha \in [0, n\phi]$, where n is the number of units that make up the actuator. Table 2 provides the specific parameter values of the rotary actuator.

Table 2. Specific parameter values

Symbol	Quantity	Values
t	Initial thickness	1.5mm
a	Off-axis distance	20mm
b	Radial width	40mm
θ	Tilt angle	30°
ϕ	Maximum angle of each unit	π/8
α	Joint angle	[0, nϕ]

To limit the rotation range of the unit, the position of the sealing line needs to be determined during fabrication. By using Eq. (13) and Eq. (14), which were derived in Section 3.3, the initial included angle η of each unit is calculated to be 5.72°, and the included angle μ between each unit is determined to be 5.67°. Therefore, through geometric relationships, it is easy to obtain RT and UV, as shown in Fig. 21(a).

$$\begin{cases} RT = (\phi + \eta) \times (a + b) \approx 29.55mm \\ UV = (\phi + \eta) \times a \approx 9.85mm \end{cases} \tag{17}$$

All angles during the operation are in radians. The arc length between two adjacent units can be calculated using the same method, and finally, the distances S_1 and S_2 between each vertex and the sealing line can be calculated, as shown in Fig. 21(b).

$$\begin{cases} S_1 \approx \frac{1}{2}(n \times UV + (n-1) \times \mu \times a) \\ S_2 \approx \frac{1}{2}(n \times RT + (n-1) \times \mu \times (a+b)) \end{cases} \tag{18}$$

A measurement platform is built to measure the various experimental parameters of the rotary actuator. A torque sensor with a range of [0, 20 Nm] and a sensitivity of 0.2% was used to measure the static torque of the actuator. The rotation angle is obtained using the SA100 GMR angle sensor with a range of [0, 360°] and a resolution of 0.09°. A JC-101AV air pressure sensor with a range of [-101 kPa, 101 kPa] and a repeatability of 0.1% was used to obtain the current air pressure value. Each sensor is installed and connected, as shown in Fig. 21(c).

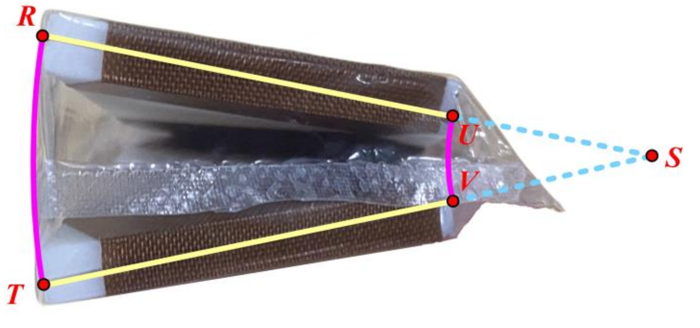

(a) The sealing parameters of each unit

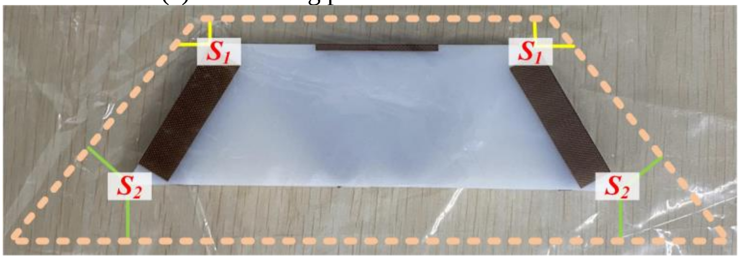

(b) The sealing line of the rotary actuator

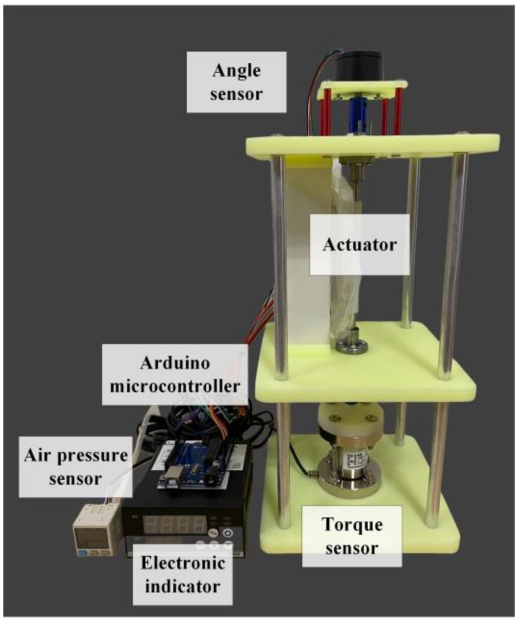

(c) Measurement platform

Fig. 21. Experimental materials

4.2. Rotation test

In Section 3.1, a novel crease design method for thick origami is proposed. It is proven that the rotation axis L_R is fixed at any joint angle. To verify the availability of this method, a rotary actuator with a unit number of n=1 is used for the rotation test. The range of the joint angles is set to [0, 2π/3], and the actuator is fixed. Air is injected into the actuator to control its folding, and a camera is used to record it at certain angles. The changes in the rotation axis L_R during the folding of the actuator are shown in Fig. 22.

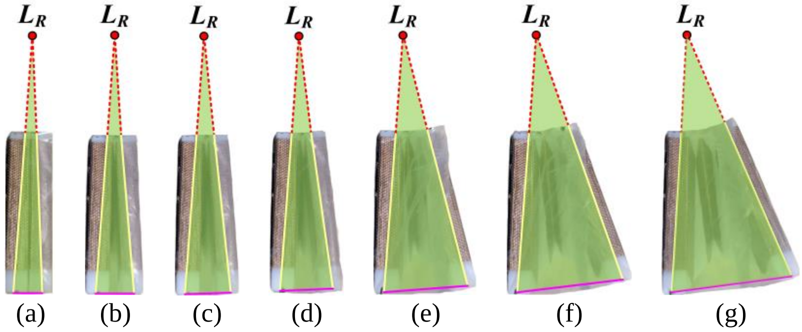

Fig. 22. Rotation test of the rotary actuator. (a)-(g) represent different joint angles.

Taking the rotation axis when the joint angle is equal to 0 as the reference axis L_{R0}, the positions of the other rotation axes can be obtained, as shown in Fig. 23(a). Moreover, the positions of the rotation axes L_R on the X-axis fall between [-0.4 mm, 0.6 mm], and the positions on the Y-axis fall between [-0.3 mm, 0.4 mm]. Then, the distances between each rotation axis L_R and the reference axis L_{R0} are calculated and plotted using the joint angle as the X-axis, as shown in Fig. 23(b). As the angle increases, the eccentric distance also increases. However, all distances do not exceed 0.7 mm. This is a deviation of only 1.17% relative to the entire actuator's radius of rotation. Within the set maximum rotation angle, there is only a deviation of less than 0.5%, which is acceptable.

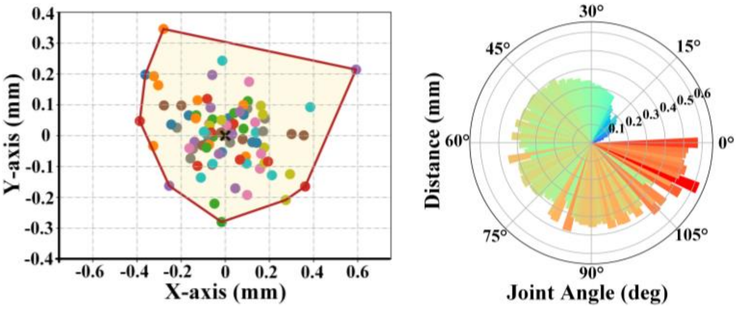

(a) Rotation error (b) Eccentric distance

Fig. 23. Rotation error of the rotary actuator under different joint angles.

4.3. Repeatability test

Repeatability is a very important performance parameter for a rotary actuator. In this paper, the actuator can reach the same position multiple times with the same volume of air injected. As shown in Figs. 23(a), 23(b), and 23(c), the repeatability test is carried out using three situations where the number of units is n=1, n=2, and n=3, while ensuring that the internal and external air pressure difference is 0 during each measurement. When n=1, the interval is 25 cc as a group, and each group is repeated 10 times until the actuator reaches the maximum angle. When n=2 and n=3, the interval is 50 cc as a group, and each group is repeated 5 times until the actuator reaches the maximum angle. As the air volume V injected into the actuator increases, the rotation angle α of the actuator will also increase. The injected air volume V and rotation angle α are recorded at the same time. The experimental results are shown in Fig. 24.

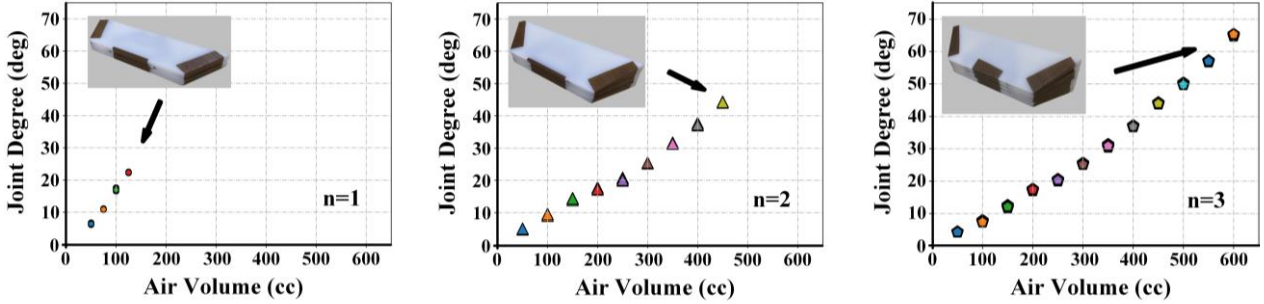

(a) n=1 (b) n=2 (c) n=3

Fig. 24. Repeatability test of the rotary actuator

It can be seen from the figure that as the injection volume V increases, the rotation angle α also increases, and the two are linearly related. As the injection volume continues to increase, the actuators in the three cases of n=1, n=2, and n=3 all reach maximum angles of 22.36°, 44.21°, and 65.34°, with only deviations of 0.62%, 1.75%, and 3.2% from the theoretical maximum angles, respectively. Then, the mean square error (MSE) operation is performed on the data of each group to analyse its degree of dispersion. The results are shown in Table 3. By, observing the results under different volumes in the table, we can see that all MSEs are less than 0.4, which shows that the rotary actuator has relatively good repeatability.

Table 3. Mean square error under different numbers of units and volumes

n=1

Volume (cc)	50	75	100	125
MSE	0.212	0.125	0.315	0.114

n=2

Volume (cc)	50	100	150	200	250	300	350	400	450
MSE	0.130	0.261	0.230	0.236	0.360	0.103	0.169	0.300	0.121

n=3

Volume (cc)	50	100	150	200	250	300	350	400	450	500	550	600
MSE	0.028	0.169	0.235	0.169	0.210	0.129	0.271	0.123	0.146	0.177	0.134	0.219

4.4. Static torque test

In Section 3.4, the relationship between the actuator's torque and pressure is derived. In this formula, k is an inherent stiffness constant, which depends on the actuator's material and structure. In this section, the inherent stiffness constant k will be determined.

To obtain the relationship between the torque and pressure, the test is conducted with n=2 units. The experiment was divided into three groups, and the rotation angle α of each group was fixed at 15°, 30° and 45°. By continuously injecting air, the torque generated by the actuator and the internal pressure will increase accordingly. The torque T and pressure difference ΔP are recorded at an interval of 0.2 kPa each time, where $\Delta P=P- P_0$. The experimental results are shown in Fig.

25(a).

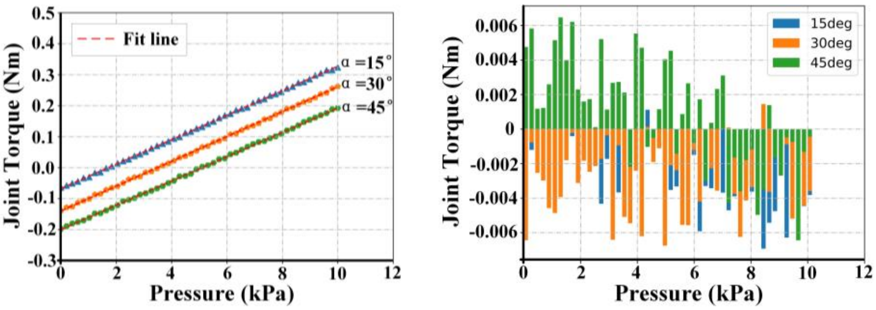

(a) Torque-Pressure (b) Experimental and theoretical errors

Fig. 25. Static torque test of the rotary actuator

We performed a linear fit on the experimental data and solved for the slopes and intercepts of the three fit lines. SI units are used in this study. When the rotation angle is α=15°, the slope and intercept of the fit line are 3.95×10^{-5} and -0.0677, respectively. When the rotation angle is α=30°, the slope and intercept of the fit line are 4.01×10^{-5} and -0.1401, respectively. When the rotation angle is α=45°, the slope and intercept of the fit line are 3.92×10^{-5} and -0.2003, respectively. According to Eq. (16), combined with the specific parameters of the actuator, the theoretical slope can be obtained as 4.00×10^{-5}. Then, based on the intercepts at different angles, the obtained inherent stiffness constant k is averaged, and the final measured value is -0.261. Using the measured inherent stiffness constant k, the error between the torque and the theoretical value under different air pressures is calculated. The results are shown in Fig. 25(b). It can be observed that the error only occurs between -0.008 Nm and 0.008 Nm, which verifies the accuracy of the model.

5. Conclusion

In this paper, a novel synthesis approach of origami-inspired mechanisms based on graph theory is proposed. The core idea of this approach is to equate the synthesis of the origami mechanism to the synthesis of the generalized parallel mechanism. First, all contracted graphs that satisfy the requirements are listed by analysing the degrees of freedom and motion characteristics of the designed origami mechanism. Then, loop synthesis is carried out on the contracted graphs of the origami mechanism. To verify the availability of the loop situations, two theorems are proposed in this paper, resulting in 72 valid loop situations. Moreover, one of the loop situations is selected to complete the design of the origami mechanism. Consequently, a modified method to design thick origami is introduced in this paper. Finally, a rotary actuator is manufactured by wrapping the above origami mechanism with PVC film, and the inherent stiffness constant of the actuator is measured through tests of rotation, repeatability, and static torque. Thus, the validity of the novel synthesis approach proposed in this paper is verified.

Declaration of Competing Interest

We declare that we have no financial and personal relationships with other people or organizations that can inappropriately influence our work, there is no professional or other personal interest of any nature or kind in any product, service and/or company that could be construed as influencing the position presented in, or the review of, the manuscript entitled.

Acknowledgments

The authors gratefully acknowledge the financial support of the National Nature Science Foundation of China under grants 52150710538 and 52305012.

References

[1] B. Sargent, J. Butler, K. Seymour, et al., An origami-based medical support system to mitigate flexible shaft buckling. Journal of Mechanisms and Robotics, 2020, 12(4): 041005.

[2] Y. Lin, G. Yang, Y. Liang, et al., Controllable stiffness origami "skeletons" for lightweight and multifunctional artificial muscles. Advanced Functional Materials, 2020, 30(31): 2000349.

[3] T. H. Kim, J. Vanloo, W. S. Kim, 3D origami sensing robots for cooperative healthcare monitoring. Advanced Materials Technologies, 2021, 6(3): 2000938.

[4] B. Liu, Y. Liao, Y. Yang, et al., Design and analysis of reconfigurable and deployable thin-walled architectural equipment inspired by Mirror-Miura origami patterns. Engineering Structures, 2023, 286: 116059.

[5] A. A. Deleo, J. O'Neil, H. Yasuda, et al., Origami-based deployable structures made of carbon fiber reinforced polymer composites. Composites Science and Technology, 2020, 191: 108060.

[6] M. Meloni, J. Cai, Q. Zhang, et al., Engineering origami: A comprehensive review of recent applications, design methods, and tools. Advanced Science, 2021, 8(13): 2000636.

[7] S. Mintchev, M. Salerno, A. Cherpillod, et al., A portable three-degrees-of-freedom force feedback origami robot for

human–robot interactions. Nature Machine Intelligence, 2019, 1(12): 584-593.

[8] H. Dong, H. Yang, S. Ding, et al., Bioinspired amphibious origami robot with body sensing for multimodal locomotion. Soft Robotics, 2022, 9(6): 1198-1209.

[9] Q. Zhang, H. Fang, J. Xu, Yoshimura-origami based earthworm-like robot with 3-dimensional locomotion capability. Frontiers in Robotics and AI, 2021, 8: 738214.

[10] H. Bhardwaj, X. Cai, L. S. T. Win, et al., Nature-inspired in-flight foldable rotorcraft. Bioinspiration & Biomimetics, 2023, 18(4): 046012.

[11] W. Cha, M. F. Campbell, G. A. Popov, et al., Microfabricated Foldable Wings for Centimeter-Scale Microflyers. Journal of Microelectromechanical Systems, 2020, 29(5): 1127-1129.

[12] S. M. Baek, S. Yim, S. H. Chae, et al., Ladybird beetle–inspired compliant origami. Science Robotics, 2020, 5(41): eaaz6262.

[13] T. Chen, O. R. Bilal, R. Lang, et al., Autonomous deployment of a solar panel using elastic origami and distributed shape-memory-polymer actuators. Physical Review Applied, 2019, 11(6): 064069.

[14] A. Russo, Multi-functional SElf reconfigurable robotic arm (RAMSEs) and adjoined solar panel preliminary design for lunar entry approach platform for research on ground. 2020.

[15] Y. Zhang, M. Li, Y. Chen, et al., Thick-panel origami-based parabolic cylindrical antenna. Mechanism and Machine Theory, 2023, 182: 105233.

[16] K. Wang, Y. Chen, P. Wang-Iverson, et al., Folding a patterned cylinder by rigid origami. Origami, 2011, 5: 265-276.

[17] M. Savchenko, V. Savchenko, A. Abe, et al., A study on an origami-based structure for use as a sun umbrella. SN Applied Sciences, 2020, 2: 1-13.

[18] K. Miura, Method of packaging and deployment of large membranes in space. The Institute of Space Astronautical Science Report, 1985, 618: 1.

[19] R. Xie, J. Li, Y. Chen, The graded origami structures. ASME 2015 International Design Engineering Technical Conferences and Computers and Information in Engineering Conference. American Society of Mechanical Engineers, 2015: V05BT08A026.

[20] J. Ma, J. Song, Y. Chen, An origami-inspired structure with graded stiffness. International Journal of Mechanical Sciences, 2018, 136: 134-142.

[21] T. Tachi, Generalization of rigid-foldable quadrilateral-mesh origami. Journal of the International Association for Shell and Spatial Structures, 2009, 50(3): 173-179.

[22] J. Mitani, 3D Origami Art. Boca Raton: CRC Press, 2016.

[23] T. A. Evans, R. J. Lang, S. P. Magleby, et al., Rigidly foldable origami twists. Origami, 2015, 6: 119-130.

[24] G. Jia, H. Huang, H. Guo, et al., Design of transformable hinged ori-block dissected from cylinders and cones. Journal of Mechanical Design, 2021, 143(9): 094501.

[25] L. Li, Y. Fang, S. Guo, et al., Type synthesis of a class of novel 3-DOF single-loop parallel leg mechanisms for walking robots. Mechanism and Machine Theory, 2020, 145: 103695.

[26] L. Li, Y. Fang, L. Wang, Design of a family of multi-DOF drive systems for fewer limb parallel mechanisms. Mechanism and Machine Theory, 2020, 148: 103802.

[27] C. Tian, D. Zhang, H. Tang, et al., Structure synthesis of reconfigurable generalized parallel mechanisms with configurable platforms. Mechanism and Machine Theory, 2021, 160: 104281.

[28] C. Tian, Y. Fang, Q. J. Ge, Design and analysis of a partially decoupled generalized parallel mechanism for 3T1R motion. Mechanism and Machine Theory, 2019, 140: 211-232.

[29] C. M. Feng, T. S. Liu, A graph-theory approach to designing deployable mechanism of reflector antenna. Acta Astronautica, 2013, 87: 40-47.

[30] C. Tian, Y. Fang, Q. J. Ge, Structural synthesis of parallel manipulators with coupling sub-chains. Mechanism and Machine Theory, 2017, 118: 84-99.

[31] L. He, H. Fang, D. Zhang, Design of a class of reconfigurable hybrid mechanisms for large complex curved surface machining based on topological graph theory. Mechanism and Machine Theory, 2023, 190: 105461.

[32] Y. Yang, P. Li, H. Pei, et al., Design of all-wheel-drive power-split hybrid configuration schemes based on hierarchical topology graph theory. Energy, 2022, 242: 122944.

[33] G. Jia, H. Huang, B. Li, et al., Synthesis of a novel type of metamorphic mechanism module for large scale deployable grasping manipulators. Mechanism and Machine Theory, 2018, 128: 544-559.

[34] G. Jia, B. Li, H. Huang, et al., Type synthesis of metamorphic mechanisms with scissor-like linkage based on different kinds of connecting pairs. Mechanism and Machine Theory, 2020, 151: 103848.

[35] G. Jia, H. Huang, S. Wang, et al., Type synthesis of plane-symmetric deployable grasping parallel mechanisms using constraint force parallelogram law. Mechanism and Machine Theory, 2021, 161: 104330.

[36] J. Dai, D. G. Caldwell. Origami-based robotic paper-and-board packaging for food industry. Trends in food science & technology, 2010, 21(3): 153-157.

[37] Y. Lu, T. Leinonen, Type synthesis of unified planar–spatial mechanisms by systematic linkage and topology matrix-graph technique. Mechanism and Machine Theory, 2005, 40(10): 1145-1163.

[38] Z. Huang, Y. Zhao, T. Zhao, Advanced Spatial Mechanism, China Higher Education Press, Beijing, 2006.

[39] Z. Xia, D. Zhang, Y. Chen, et al., A novel 6 DOFs generalized parallel manipulator design and analysis based on humanoid leg. Mechanism and Machine Theory, 2022, 176: 105029.
[40] K. Miura, Method of packaging and deployment of large membranes in space. The Institute of Space and Astronautical Science report, 1985, 618: 1-9.
[41] E. D. Demaine, J. O'Rourke, Geometric folding algorithms: linkages, origami, polyhedra. Cambridge university press, 2007.
[42] T. Tachi, Rigid-foldable thick origami. Origami, 2011, 5: 253-264.
[43] Y. Chen, R. Peng, Z. You, Origami of thick panels. Science, 2015, 349(6246): 396-400.
[44] R. J. Lang, L. L. Howell, Laminar emergent flexural fold joints: Planar compliant mechanisms with large-angle near-revolute motion. Extreme Mechanics Letters, 2022, 52: 101657.
[45] S. Li, D. M. Vogt, D. Rus, et al., Fluid-driven origami-inspired artificial muscles. Proceedings of the National academy of Sciences, 2017, 114(50): 13132-13137.

Appendix Ⅰ：

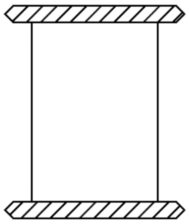
1-1

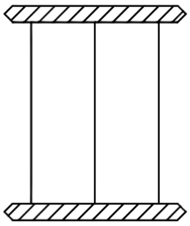
2-1

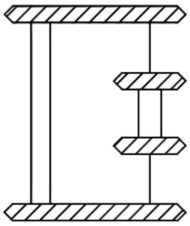
3-1

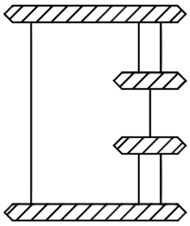
3-2

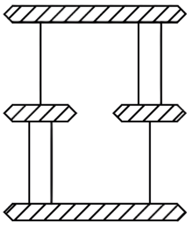
3-3

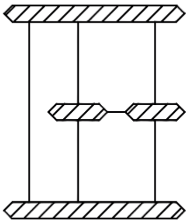
3-4

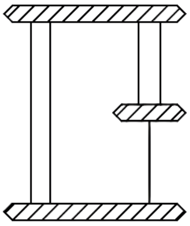
3-5

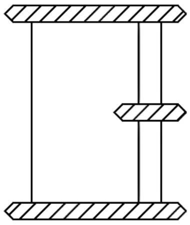
3-6

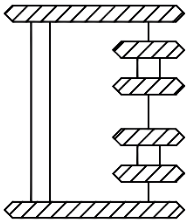
4-1

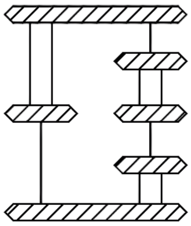
4-2

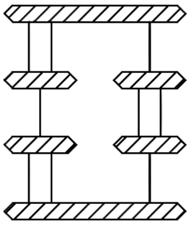
4-3

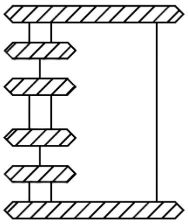
4-4

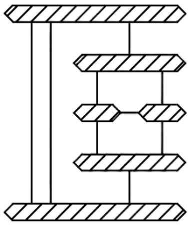
4-5

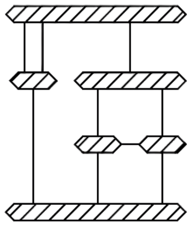
4-6

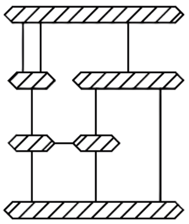
4-7

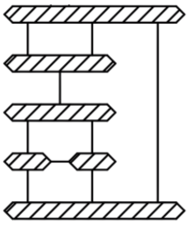
4-8

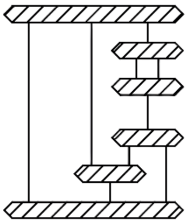
4-9

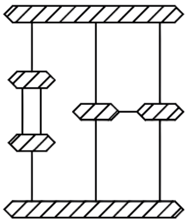
4-10

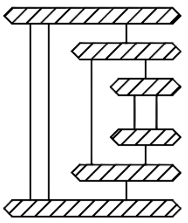
4-11

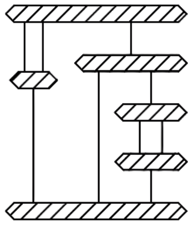
4-12

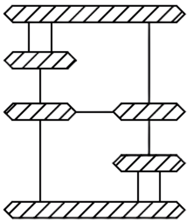
4-13

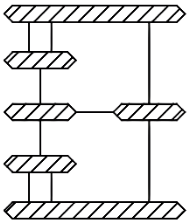
4-14

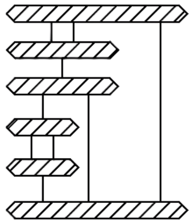
4-15

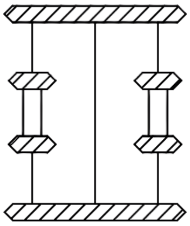
4-16

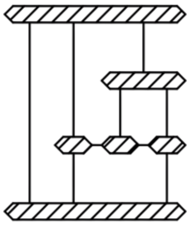
4-17

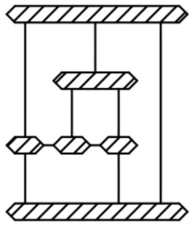
4-18

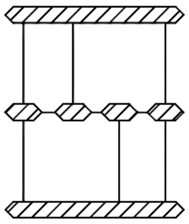
4-19

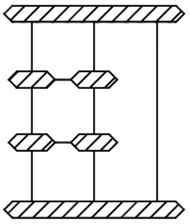
4-20

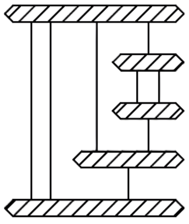
4-21

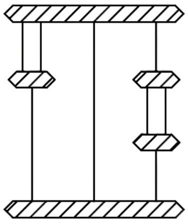
4-22

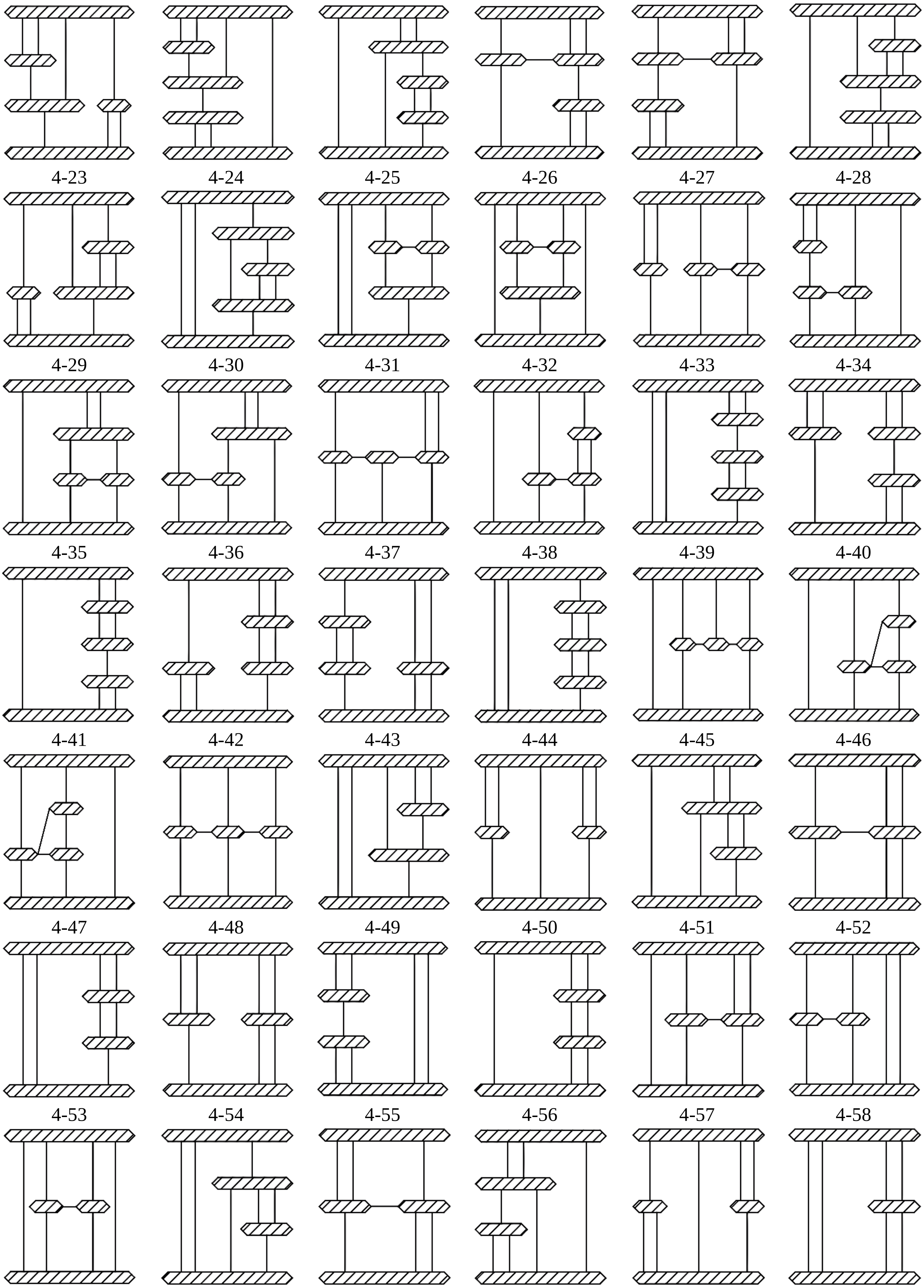
4-23 4-24 4-25 4-26 4-27 4-28
4-29 4-30 4-31 4-32 4-33 4-34
4-35 4-36 4-37 4-38 4-39 4-40
4-41 4-42 4-43 4-44 4-45 4-46
4-47 4-48 4-49 4-50 4-51 4-52
4-53 4-54 4-55 4-56 4-57 4-58
4-59 4-60 4-61 4-62 4-63 4-64

72 available loop situations